Draft version March 15, 2021
Typeset using LaTeX twocolumn style in AASTeX63



# SCExAO/MEC and CHARIS Discovery of a Low Mass, 6 AU-Separation Companion to HIP 109427 using Stochastic Speckle Discrimination and High-Contrast Spectroscopy*

Sarah Steiger,[1] Thayne Currie,[2,3,4] Timothy D. Brandt,[1] Olivier Guyon,[2,5,6,7] Masayuki Kuzuhara,[7,8] Jeffrey Chilcote,[9] Tyler D. Groff,[10] Julien Lozi,[2] Alexander B. Walter,[11] Neelay Fruitwala,[1] John I. Bailey, III,[1] Nicholas Zobrist,[1] Noah Swimmer,[1] Isabel Lipartito,[1] Jennifer Pearl Smith,[1] Clint Bockstiegel,[12] Seth R. Meeker,[11] Gregoire Coiffard,[1] Rupert Dodkins,[1] Paul Szypryt,[13,14] Kristina K. Davis,[1] Miguel Daal,[1] Bruce Bumble,[11] Sebastien Vievard,[2] Ananya Sahoo,[2] Vincent Deo,[2] Nemanja Jovanovic,[15] Frantz Martinache,[16] Motohide Tamura,[7,8,17] N. Jeremy Kasdin,[18] and Benjamin A. Mazin[1]

[1]*Department of Physics, University of California, Santa Barbara, Santa Barbara, California, USA*
[2]*Subaru Telescope, National Astronomical Observatory of Japan, 650 North A'ohōkū Place, Hilo, HI 96720, USA*
[3]*NASA-Ames Research Center, Moffett Blvd., Moffett Field, CA, USA*
[4]*Eureka Scientific, 2452 Delmer Street Suite 100, Oakland, CA, USA*
[5]*Steward Observatory, The University of Arizona, Tucson, AZ 85721, USA*
[6]*College of Optical Sciences, University of Arizona, Tucson, AZ 85721, USA*
[7]*Astrobiology Center of NINS, 2-21-1, Osawa, Mitaka, Tokyo, 181-8588, Japan*
[8]*National Astronomical Observatory of Japan, 2-21-2, Osawa, Mitaka, Tokyo 181-8588, Japan*
[9]*Department of Physics, University of Notre Dame, South Bend, IN, USA*
[10]*NASA-Goddard Space Flight Center, Greenbelt, MD, USA*
[11]*Jet Propulsion Laboratory, California Institute of Technology, Pasadena, California 91125, USA*
[12]*CERN - 1211 Geneva 23 - Switzerland*
[13]*National Institute of Standards and Technology, Boulder, Colorado 80305, USA*
[14]*Department of Physics, University of Colorado, Boulder, Colorado 80309, USA*
[15]*Department of Astronomy, California Institute of Technology, 1200 E. California Blvd.,Pasadena, CA, 91125, USA*
[16]*Université Côte d'Azur, Observatoire de la Côte d'Azur, CNRS, Laboratoire Lagrange, France*
[17]*Department of Astronomy, Graduate School of Science, The University of Tokyo, 7-3-1, Hongo, Bunkyo-ku, Tokyo, 113-0033, Japan*
[18]*University of San Francisco, San Francisco, CA 94118*

## ABSTRACT

We report the direct imaging discovery of a low-mass companion to the nearby accelerating A star, HIP 109427, with the Subaru Coronagraphic Extreme Adaptive Optics (SCExAO) instrument coupled with the MKID Exoplanet Camera (MEC) and CHARIS integral field spectrograph. CHARIS data reduced with reference star PSF subtraction yield 1.1–2.4 µm spectra. MEC reveals the companion in $Y$ and $J$ band at a comparable signal-to-noise ratio using stochastic speckle discrimination, with no PSF subtraction techniques. Combined with complementary follow-up $L_{\mathrm{p}}$ photometry from Keck/NIRC2, the SCExAO data favors a spectral type, effective temperature, and luminosity of M4–M5.5, 3000-3200 $K$, and $\log_{10}(L/L_{\odot}) = -2.28^{+0.04}_{-0.04}$, respectively. Relative astrometry of HIP 109427 B from SCExAO/CHARIS and Keck/NIRC2, and complementary Gaia-Hipparcos absolute astrometry of the primary favor a semimajor axis of $6.55^{+3.0}_{-0.48}$ au, an eccentricity of $0.54^{+0.28}_{-0.15}$, an inclination of $66.7^{+8.5}_{-14}$ degrees, and a dynamical mass of $0.280^{+0.18}_{-0.059}$ $M_{\odot}$. This work shows the potential for extreme AO systems to utilize speckle statistics in addition to widely-used post-processing methods to directly image faint companions to nearby stars near the telescope diffraction limit.

Corresponding author: Sarah Steiger
steiger@ucsb.edu

* Based in part on data collected at Subaru Telescope, which is operated by the National Astronomical Observatory of Japan.

# 1. INTRODUCTION

Nearly all of the $\sim$ 10–20 directly imaged planets discovered so far orbit their host stars at 10–150 au separations, typically $\rho \sim 0\farcs4$–$2''$ on the sky (e.g. Marois et al. 2008b; Lagrange et al. 2009; Rameau et al. 2013; Kuzuhara et al. 2013; Currie et al. 2014; Macintosh et al. 2015; Chauvin et al. 2017). The first generation of extreme adaptive optics (AO) instruments, such as the Gemini Planet Imager (GPI; Macintosh et al. 2014) and the Spectro-Polarimetric High-contrast Exoplanet REsearch at VLT (SPHERE; Beuzit et al. 2019), have achieved factors of 100 improvement in contrast at sub-arcsecond separations over conventional systems, but typically were only sensitive to jovian exoplanets at projected separations beyond $\sim$ 10 au (e.g. Nielsen et al. 2019; Vigan et al. 2020). To more frequently identify companions at Jupiter-to-Saturn separations, upgraded versions of GPI/SPHERE and second-generation systems like SCExAO and MagAO-X (Jovanovic et al. 2015b; Males et al. 2020) must yield deeper contrasts at $\rho < 0\farcs4$.

Point spread function (PSF) sized speckles with a range of correlation timescales ($\tau$) and sources currently limit achievable contrasts from the ground. Rapidly-evolving atmospheric speckles ($\tau \sim$ 1-20 ms) result from aberrations left uncorrected by an AO system and average out over the course of long-exposure images, forming a smooth halo (e.g. Perrin et al. 2003; Soummer et al. 2007). These "fast" speckles can be corrected by improved AO control loops which will mitigate temporal bandwidth error and measurement (photon noise) error (e.g. Guyon 2005). Alternatively, quasi-static speckles result from imperfections in the instrument such as non-common path errors, telescope vibrations, the finite speed of the AO loop, etc. (Guyon 2005; Lozi et al. 2018). These speckles interfere with atmospheric speckles and can be pinned to the diffraction rings (Soummer et al. 2007). Quasi-static speckle noise follows a highly non-Gaussian (modified Rician distribution) and is temporally well correlated ($\tau \sim$ 10-60 minutes), presenting a fundamental obstacle in exoplanet direct imaging (e.g. Marois et al. 2008a).

While focal-plane wavefront control methods can conceivably suppress these speckles (e.g. Give'on et al. 2007), post-processing methods provide the most common way of removing them. Unfortunately, common post-processing techniques utilizing advanced PSF subtraction methods (e.g. Lafrenière et al. 2007; Soummer et al. 2012) become less effective at small angles where direct detections are most challenging. Angular Differential Imaging (ADI; Marois et al. 2006) exploits parallactic angle (PA) rotation; however, the rotation in $\lambda$/D units is smaller within a few diffraction beamwidths, resulting in severe self-subtraction of a planet signal (Mawet et al. 2012). Similarly, Spectral Differential Imaging (SDI; Marois et al. 2000) utilizes the wavelength-independent nature of phase-induced speckle noise to rescale (magnify) slices of polychromatic images. However, SDI requires broad spectral coverage close to the primary otherwise it also suffers from self-subtraction effects. Reference Star Differential Imaging (RDI/RSDI; Soummer et al. 2012) does not inherently suffer at small inner working angles (IWAs), but requires careful magnitude and color matching between the target of interest and the reference star. A method to suppress quasi-static speckles that is free of the limitations of ADI, SDI, and RDI would significantly improve our ability to detect jovian planets at Jupiter-to-Saturn like separations.

Here we demonstrate the use of a post-processing technique called Stochastic Speckle Discrimination (SSD; Gladysz & Christou 2008; Meeker et al. 2018; Fitzgerald & Graham 2006) for detecting new low mass companions using SCExAO and the Microwave Kinetic Inductance Detector (MKID) Exoplanet Camera (MEC; Walter et al. 2020). SSD works by utilizing the timing resolution of MKID detectors to break up an observation into a series of short exposures. This allows us to then sample the underlying probability density function (PDF) that describes the off-axis intensity in an image (light from a speckle) which can be written analytically as a modified Rician distribution. Fitting this distribution to each pixel in one of the short exposure images allows us to diagnose whether a bright point in an image is a quasi-static speckle or a true companion, see Section 3.1.2.

We also report the discovery of a low mass stellar companion to HIP 109427 using, in part, SSD with SCExAO/MEC. We also utilize SCExAO/MEC photometry, SCExAO/CHARIS spectroscopy, and Keck/NIRC2 photometry. This companion has a best fit dynamical mass of $\sim 0.25\ M_{\odot}$ consistent with a spectral type of M4–M5.5 from spectral analysis.

This discovery serves as an important proof-of-concept for the use of time-domain information in addition to standard PSF subtraction methods exploiting spectral and spatial information to remove quasi-static speckles in high-contrast images.

# 2. SYSTEM PROPERTIES AND OBSERVATIONS

HIP 109427 (tet Peg) is a nearby ($d$ = 28.3 pc) $\lambda$ Boo star with a spectral type of A1V (van Leeuwen 2007; Gray et al. 2006). David & Hillenbrand (2015) and Stone et al. (2018) derive system ages of $t \sim$ 400–

**Table 1.** HIP 109427 Observing Log

| UT Date | Instrument | coronagraph | Seeing ($''$) | Passband | $\lambda$ ($\mu m$)[a] | $t_{\rm exp}$ (s) | $N_{\rm exp}$ | $\Delta$PA ($^o$) | Post-Processing Strategy |
|---|---|---|---|---|---|---|---|---|---|
| **New Data** | | | | | | | | | |
| 20200731 | SCExAO/CHARIS | Lyot | 0.6 | $JHK$ | 1.16–2.37 | 10.32 | 43 | 5.4 | RDI/KLIP |
| 20201007 | SCExAO/MEC | Lyot | 0.35 | $YJ$ | 0.95–1.14 | 25.0 | 36 | 2.3 | SSD |
| – | SCExAO/CHARIS | Lyot | 0.35 | $H$ | 1.48–1.79 | 16.23-20.65[b] | 78 | 5.4 | none |
| 20201225 | Keck/NIRC2+PyWFS | none | 0.7 | $Lp$ | 3.78 | 22.5 | 49 | 3.5 | RDI/KLIP |
| **Archival Data** | | | | | | | | | |
| 20151028 | Keck/NIRC2 | vortex | 0.7 | $Lp$ | 3.78 | 25 | 25 | 11.6 | RDI/ALOCI |

Note—a) For CHARIS and MEC data, this column refers to the wavelength range. For broadband imaging data, it refers to the central wavelength. b) Total integration time is 1524 $s$.

700 Myr; Banyan-$\Sigma$ does not reveal evidence that the star's kinematics are consistent with younger moving groups (Gagné et al. 2018). While HIP 109427 lacks a published detected radial-velocity trend indicative of a companion (Lagrange et al. 2009; Howard & Fulton 2016), Makarov & Kaplan (2005) suggest evidence for a potential companion at a 5.7$\sigma$ level from Hipparcos astrometry. Previous direct imaging observations taken as a part of the thermal infrared LEECH survey conducted with the Large Binocular Telescope failed to image any companions (Stone et al. 2018). Searches through public archives show that the star has not been targeted as a part of the Gemini Planet Imager campaign planet search, but it has been observed with VLT/NaCo and SPHERE without a reported companion.

Astrometry derived from the *Hipparcos-Gaia Catalogue of Accelerations* (HGCA; Brandt 2018) reveals a substantial deviation from simple linear kinematic motion ($\chi^2$ = 108.83) consistent with a $\sim$ 11-$\sigma$-significant acceleration. We therefore targeted this star as a part of our survey to discover low-mass companions to accelerating stars (e.g. Currie et al. 2020a).

In three epochs between July and December 2020, we observed HIP 109427 with the Subaru Telescope using SCExAO coupled to CHARIS and MEC and with the Keck II telescope using the NIRC2 camera. An AO correction was provided by the near-IR Pyramid wavefront sensor (PyWFS; Jovanovic et al. 2015b; Currie et al. 2020b; Groff et al. 2016; Walter et al. 2020; Bond et al. 2020) (Table 1). Conditions were photometric each night with average to excellent optical seeing ($\theta_{\rm V}$ = $0\farcs35$–$0\farcs7$).

The SCExAO Pyramid wavefront sensor ran at 2 kHz, correcting for 1080 spatial modes and achieving a high-fidelity AO correction. MEC data (7 October 2020) covers wavelengths over the $Y$ and $J$ passbands (0.95 - 1.4 µm) at a spectral resolution of $\mathcal{R} \sim 3.3$. We obtained CHARIS data in broadband (31 July 2020) at a resolution of $\mathcal{R} \sim 18$ or in $H$ band at a higher resolution ($\mathcal{R} \sim 70$). The Keck PyWFS corrected the wavefront at 1 kHz, correcting for 349 spatial modes and NIRC2 data (25 December 2020) was taken in the $L_{\rm p}$ broadband filter ($\lambda_o$ = 3.78 µm).

All observations were conducted in "vertical angle"/pupil tracking mode, enabling angular differential imaging (ADI; Marois et al. 2006). The CHARIS data also enables spectral differential imaging (SDI; Marois et al. 2000). CHARIS and MEC data utilized the Lyot coronagraph ($0\farcs23$ diameter) to suppress the stellar halo, as well as satellite spots for precise astrometric and spectrophotometric calibration (e.g. Jovanovic et al. 2015a; Currie et al. 2018a; Sahoo et al. 2020). NIRC2 exposures left the HIP 109427 primary unocculted and unsaturated. Parallactic angle rotation for all data sets was small to negligible; however, we obtained reference star observations for the CHARIS broadband and NIRC2 data (HIP 105819 and HIP 112029, respectively).

To complement these new data, we analyzed Keck/NIRC2 $L_{\rm p}$ data for HIP 109427 taken on 28 October 2015 from the Keck Observatory Archive (Program ID C197NI). These data were obtained with Keck II's facility (Shack-Hartmann) adaptive optics system and the vector vortex coronagraph (Serabyn et al. 2017). We used HD 212061, observed immediately after HIP 109427, for reference star subtraction.

## 3. DATA

### 3.1. *MEC Imaging Processing*

#### 3.1.1. *Basic Processing*

MEC data was reduced using the MKID Data Reduction and Analysis Pipeline (Walter et al. 2020)[1]. This pipeline notably includes a wavelength calibration, a flat-field correction, and a spectrophotometric calibration amongst other steps. The MKID Pipeline can out-

[1] GitHub: https://github.com/MazinLab/MKIDPipeline

put calibrated images in a fits file format to be able to interface with traditional post processing techniques and astronomical image viewing software, but can also output microsecond precision, time-tagged photon lists due to the unique nature of MKID detectors. For more details on MKIDs, see Szypryt et al. (2017); Mazin et al. (2012). This precise timing information allows MKID instruments like MEC to perform more unique post processing techniques like Stochastic Speckle Discrimination (SSD) as described below.

As with the CHARIS data, satellite spots were used for the spectrophotometric calibration reference. We adopted the scaling between modulation amplitude and contrast from Currie et al. (2018b) to generate the expected satellite spot flux values per passband. A stellar spectrum from the PHOENIX stellar library appropriate for an A1V star was used and the data normalized to match HIP 109427's reported J band flux (Ducati 2002). Given MEC's low energy resolution, we focused on broadband MEC photometry (not spectra). Additionally, due to the wavelength scaling of the spots, the satellite spots are extended out into elongated streaks instead of appearing as copies of an unocculted stellar PSF. This is similar to the case for GPI's polarimetry mode.

To derive photometry for the satellite spots, we therefore follow similar methods to those outlined for GPI's polarimetry mode from Millar-Blanchaer et al. (2016). Briefly, we subtract off a plane fitted background from a region surrounding each of the four satellite spots. We then use a "racetrack aperture" to extract satellite photometry, where the aperture radius (width perpendicular to the line connecting the spot and the star) equals that for the diffraction limit at the center wavelength for each wavelength bin (i.e. for $Y$ or $J$ band). The aperture radial elongation is determined empirically using the start and stop wavelengths of the bin. Photometric errors consider the intrinsic SNR of the detection, the SNR of the satellite spots, and flat-fielding errors.

#### 3.1.2. *Stochastic Speckle Discrimination (SSD) Analysis*

Stochastic Speckle Discrimination (SSD) is a post-processing technique first demonstrated by Gladysz & Christou (2008) that takes advantage of the photon counting ability of MKIDs to distinguish between speckles and faint companions in coronagraphic images that relies solely on photon arrival time statistics.

Originally derived by Goodman (1975), and experimentally verified by Cagigal & Canales (2001) and Fitzgerald & Graham (2006), the underlying probability density function that estimates the intensity distribution of off-axis stellar speckles in the image plane can be given by a modified Rician (MR)

$$p_{MR}(I) = \frac{1}{I_S} \exp\left(-\frac{I + I_C}{I_S}\right) I_0\left(\frac{2\sqrt{I I_C}}{I_S}\right) \quad (1)$$

where $I_0(x)$ denotes the zero-order modified Bessel function of the first kind, $I_C$ describes the coherent intensity component attributed to the unaberrated PSF of the primary, and $I_S$ is the time variable component of the total intensity that describes the speckle field (see also Marois et al. 2008a).

For a sequence of exposures shorter than the decorrelation time of atmospheric speckles ($\sim$ 10 ms), a histogram of the image plane intensity follows a MR: $I_C$ and $I_S$ determined for each pixel in an image (Fitzgerald & Graham 2006). Because MEC stores the arrival time information of every photon, all time binning can be done in post-processing, which is important since the bin size that ideally samples the MR distribution is difficult to determine a priori and may vary across the image.

While the individual components of the MR distribution themselves do not inherently describe the signal from a faint companion, the *ratio* of the coherent component to time variable component, $I_C/I_S$, may reveal faint companions from a comparably bright speckle field (Gladysz & Christou 2009; Meeker et al. 2018). This is because the light from a companion will generally be added to $I_C$, making this ratio larger at the location of a faint companion than the surrounding pixels.

We wrote an SSD analysis code to interface with the MKID Pipeline, whcih breaks up a MEC observation into a series of short-exposure images. Given a user-defined bin size, we then fit a MR distribution to the histogram of the intensities for each pixel using a maximum likelihood approach. Detector dithers mitigated the large number of dead pixels in the current (engineering grade) MEC array. The SSD code is run on a single dither position at a time, and the resulting $I_C$ and $I_S$ images are drizzled together into a combined image using an adaptation of the STScI DrizzlePac software package (Gonzaga et al. 2012).

We used this SSD code to process our 15 minute observation of HIP 109427 taken on 7 October 2020 to generate the image in Figure 1. For this analysis, a conservative bin size of 10 ms was chosen. The companion is clearly visible. Dark circular regions close to the edge of the coronagraph represent pinned speckles that have been suppressed by SSD due to their large $I_S$ component.

To quantify the power of this technique, we calculated the SNR by performing aperture photometry on

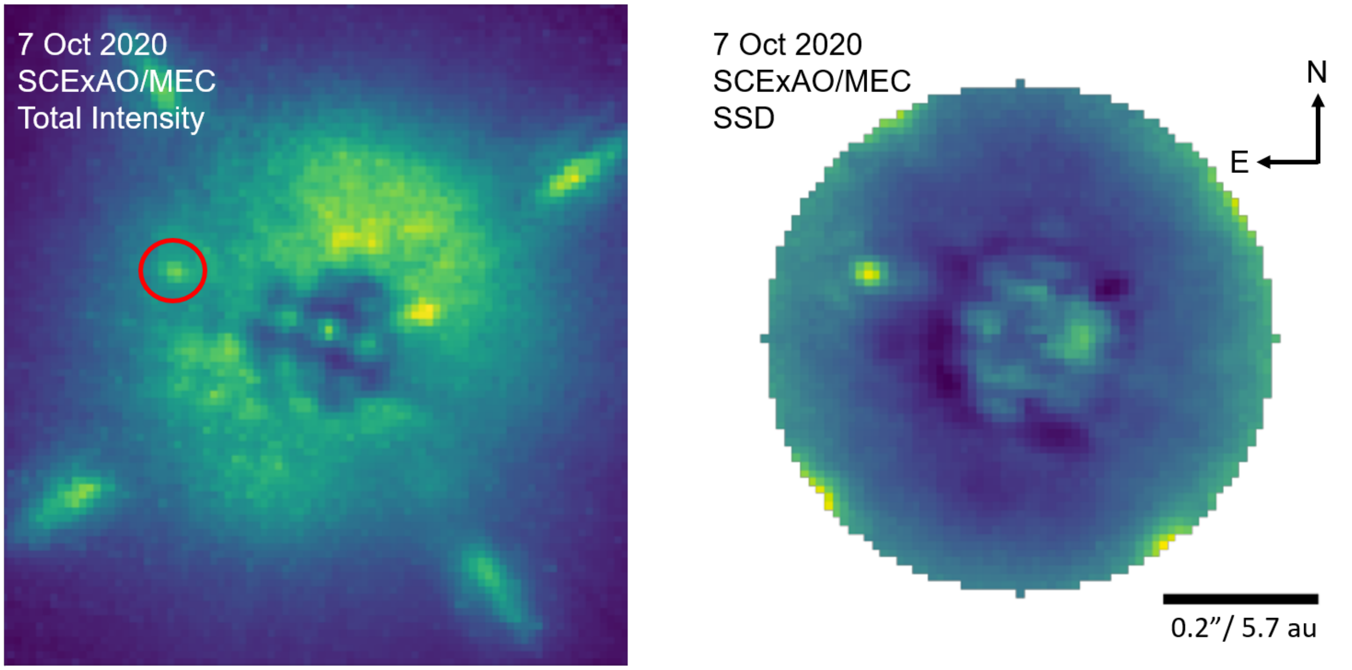


**Figure 1.** Left: Total intensity image of HIP 109427 B taken with SCExAO/MEC at $Y$ and $J$ band where the location of the companion has been circled in red. Right: SSD $I_C/I_S$ image of HIP 109427 B. Here the companion is plainly visible as well as dark regions at the edge of the coronagraph showing the removal of pinned speckles from the total intensity image.

the companion as well as at a series of locations at the same angular separation from the host star. The standard deviation of the sky-subtracted flux in each of these apertures not containing the companion was chosen to represent the noise (see also Currie et al. 2011; Mawet et al. 2014). This procedure was performed for both the total intensity and SSD decomposed images of HIP 109427 B. The SNR of the SSD image ($I_C/I_S$) is 21.4, about a factor of 3 higher than the SNR of 7 found for the total intensity image.

### 3.2. *Image Processing: CHARIS and NIRC2*

We extracted CHARIS data cubes from the raw data using the standard CHARIS pipeline (Brandt et al. 2017). To perform basic reduction steps – sky subtraction, image registration, and spectrophotometric calibration. For spectrophotometric calibration, we adopted a Kurucz stellar atmosphere model appropriate for an A1V star. For NIRC2 data, a well-tested general purpose high-contrast ADI broadband imaging pipeline (Currie et al. 2011) performed basic processing. To subtract the PSF for CHARIS broadband data and December 2020 NIRC2 $L_{\rm p}$ data, we used a full-frame implementation of reference star differential imaging (RDI) using the *Karhunen-Loe've Image Projection* (KLIP; Soummer et al. 2012) algorithm as in Currie et al. (2019), although results obtained with A-LOCI were similar (Currie et al. 2012, 2015). For the 2015 NIRC2 data, we used a full-frame version of A-LOCI.

Figure 2 shows detections of HIP 109427 B in each 2020 data set. The SNRs of HIP 109427 B in the CHARIS wavelength-collapsed broadband and $H$ band images and 2020 NIRC2 image are ~ 19, 15, and 12, respectively. HIP 109427 B is easily visible in each CHARIS channel. We failed to obtain a decisive detection of HIP 109427 B in the 2015 NIRC2 data. No other companions are seen in the field-of-view for any data set.

## 4. ANALYSIS

### 4.1. *HIP 109427 B Spectroscopy and Photometry*

For the CHARIS broadband data, we corrected for algorithm signal loss induced by KLIP using forward-modeling as described in Pueyo (2016). Because we subtracted the PSF using a reference star, only over-subtraction (not self-subtraction terms) attenuates the companion signal flux and throughput is high (~95–97%). No throughput correction is applied for the $H$ band data since we simply subtracted a median radial profile in each channel. The longest wavelength channel for the $H$ band spectrum was deemed unreliable due to extremely poor throughput and a large dispersion (a factor of 3) in the satellite spot flux densities used to map between counts and physical units ($mJy$).

Figure 3 (top panel) shows the CHARIS spectrum. The broadband and $H$ band flux densities agree to within 1-$\sigma$ except at ~ 1.45 µm, where telluric absorption is strongest. The CHARIS spectra show clear local

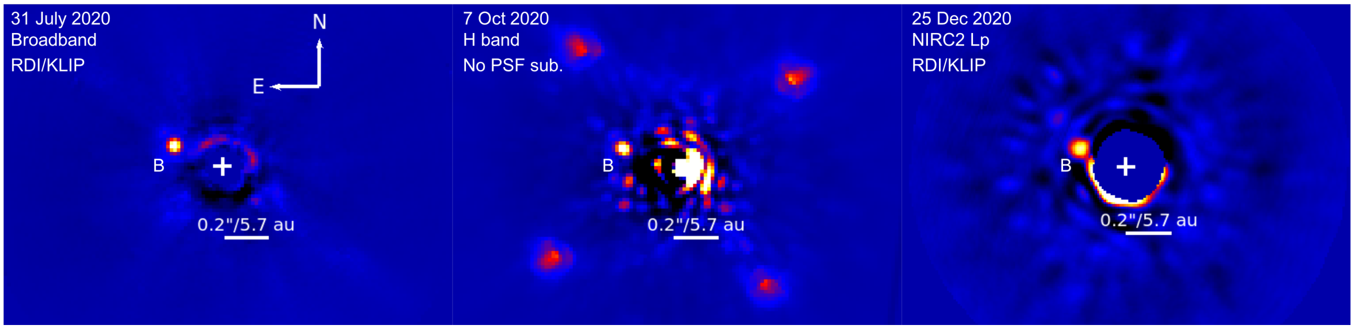


**Figure 2.** Detections of HIP 109427 B from SCExAO/CHARIS in broadband ($JHK$) and $H$ band and Keck/NIRC2 in $L_{\rm p}$. For the CHARIS broadband data (NIRC2 $L_{\rm p}$ data), we retained 5 (3) KL modes for PSF subtraction but obtain similar results for other settings.

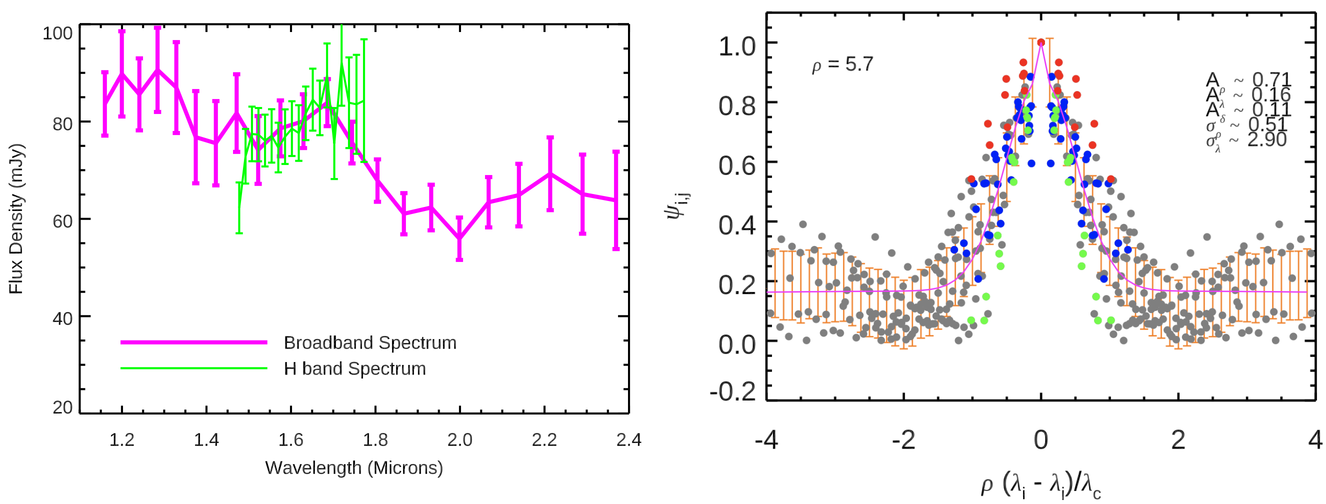


**Figure 3.** (left) SCExAO/CHARIS spectra for HIP 109427 B extracted from broadband data (magenta) and in $H$ band (green). (right) Spectral covariance for the CHARIS broadband data. The magenta line shows our fit to the spectral covariance as a function of scaled separation – $\rho(\lambda_{\rm i}$-$\lambda_{\rm j})/\lambda_{\rm c}$ – where $\rho$ is the separation in $\lambda$/D units for the central wavelength $\lambda_{\rm c}$ (see Greco & Brandt 2016). Blue, red, and green circles denote individual measurements between channels within the same major near-IR filter ($J$, $H$, or $K_{\rm s}$) while grey circles denote other individual measurements. Orange points with error bars denote binned averages with 68% confidence intervals.

minima at 1.4 µm and 1.8–2.0 µm, consistent with absorption from water opacity (e.g. Currie et al. 2020a). In the standard Mauna Kea Observatory bandpasses, HIP 109427 B photometry drawn from the CHARIS broadband spectrum and NIRC2 imaging data is $J$ = 10.62 ± 0.10, $H$ = 10.30 ± 0.07, $K_{\rm s}$ = 10.02 ± 0.11, and $L_{\rm p}$ = 9.58±0.13. The MEC $Y$ and $J$ band photometry is consistent with CHARIS-drived values: $Y$ = 10.73±0.24 and $J$ = 10.67 ± 0.23.

### 4.2. *HIP 109427 B Spectral Type, Temperature, and Luminosity*

Following recent work (Currie et al. 2020a), we compared the CHARIS spectra for HIP 109427 B to entries in the Montreal Spectral Library[2] (e.g. Gagné et al. 2015), considering the impact of spatially and spectrally correlated noise (Greco & Brandt 2016)[3]. The CHARIS data reveal highly correlated errors (Figure 3, right panel). The spectral covariance at HD 109427 B's location includes substantial off-diagonal terms, especially for spatially-correlated noise ($A_\rho \sim 0.71$) and (to a lesser extent) residuals speckles well correlated as a function of wavelength ($A_\lambda \sim 0.16$).

As shown in Figure 4, HIP 109427 B's CHARIS spectrum is best matched by M4–M5.5 field objects (left panel). Three objects in the Montreal library yield $\chi^2_\nu \leq 1$, even with the full spectral covariance included: 2MASSJ0326-0617, 2MASSJ0854-3051, and 2MASSJ2329+032. Using the mapping between spec-

[2] https://jgagneastro.com/the-montreal-spectral-library/

[3] We do not also compare the MEC or NIRC2 photometry due to sparse coverage of the library outside of the $JHK$ passbands

**Table 2.** HIP 109427 B Detection Significance, Astrometry, and Photometry

| UT Date | Instrument | Passband | SNR[a] | [E,N]($''$) | Photometry |
|---|---|---|---|---|---|
| 20200731 | SCExAO/CHARIS | $JHK$ | 19 | [0.229, 0.100] $\pm$ [0.004, 0.004] | $J = 10.62 \pm 0.10$, $H = 10.31 \pm 0.08$, $K_s = 10.02 \pm 0.10$ |
| 20201007 | SCExAO/MEC | $YJ$ | 7.0, 21.4[b] | [0.228, 0.092] $\pm$ [0.010, 0.010] | $Y = 10.73 \pm 0.23$, $J = 10.67 \pm 0.24$ |
| – | SCExAO/CHARIS | $H$ | 15 | [0.229, 0.086] $\pm$ [0.004, 0.004] | $H = 10.28 \pm 0.09$ |
| 20201225 | Keck/NIRC2 | $L_p$ | 12 | [0.222, 0.077] $\pm$ [0.003, 0.003] | $L_p = 9.58 \pm 0.13$ |

Note—a) All HD 109427 B SNR estimates were drawn from reductions used to calculate astrometry. b) The higher SNR SSD image can be used to determine MEC astrometry only: MEC photometry is performed using the simple sequence-combined image without post-processing (SNR = 7.0).

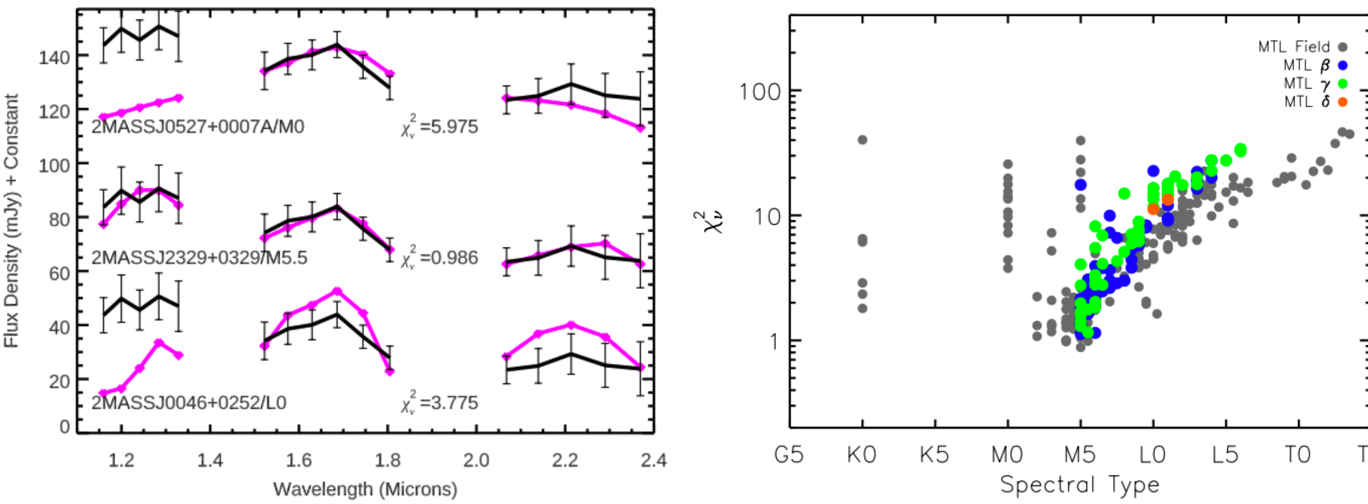


**Figure 4.** (Left) The CHARIS HIP 109427 B spectrum (black) compared to field brown dwarf spectra (magenta) with M0, M5.5, and L0 spectral types from the Montreal Spectral Library (binned to CHARIS's resolution). (Right) The $\chi^2_\nu$ distribution comparing HIP 109427 B's spectrum to objects in the Montreal Spectral Library.

tral type and effective temperature from Pecaut & Mamajek (2013), empirical comparisons to the CHARIS spectra then favor a temperature of 3000-3200 $K$ for HIP 109427 B. Adopting the relationship from Casagrande et al. (2008) and assuming a distance of 28.3 $pc$, HIP 109427 B's luminosity is $\log_{10}(L/L_\odot) = -2.28^{+0.04}_{-0.04}$.

We compared the MEC $YJ$-band photometry, CHARIS $JHK$ spectra, and NIRC2 $L_p$ photometry to the BT-Settl atmosphere models (Allard et al. 2012) with the Asplund et al. (2009) abundances downloaded from the Theoretical Spectra Web Server[4]. The grid covers temperatures of 2500–4000 $K$, surface gravities of log(g) = 3.5–5.5, and metallicities of [Fe/H] = -1 to 0.5. Following Currie et al. (2018b), we focus only on the CHARIS channels unaffected by telluric absorption, resulting in 21 photometric/spectrophotometric points fit. We define the fit quality for the $kth$ model using the $\chi^2$ statistic, considering the spectral covariance:

$$\chi^2 = R_k^T C^{-1} R_k + \sum_i (f_{phot,i} - \alpha_k\, F_{phot,ik})^2/\sigma^2_{phot,i}. \quad (2)$$

[4] http://svo2.cab.inta-csic.es/theory/newov2/

Here, the vector $R_k$ is the difference between measured and predicted CHARIS data points ($f_{spec} - \alpha_k F_{spec}$) and $C$ is the covariance for the CHARIS spectra. The vectors $f_{phot,i}$, $F_{phot,ik}$, and $\sigma_{phot,i}$ are measured photometry, model predicted photometry, and photometric uncertainty; $\alpha_k$ is the scaling factor for the model that minimizes $\chi^2$ (see also De Rosa et al. 2016).

Figure 5 shows the best-fit solar and non-solar metallicity models (top panels) and the associated $\chi^2$ contours (bottom panels). An atmosphere with a temperature of $T_{\rm eff} = 3200$ $K$ and a high gravity (log(g) = 5.5) fits the data the best in both cases. The 1-$\sigma$ contour for temperature and gravity is narrowly defined about this peak for both metallicities: $T_{\rm eff} = 3100$–$3300$ $K$ and log(g) = 5.25–5.5. At the 2-$\sigma$ level, the best-fit temperature and gravity ranges widen to 3000–3400 $K$ and log(g) = 5–5.5. The radii that minimize $\chi^2$ are ~2.1–2.6 Jupiter radii.

The best-fit solar metallicity model accurately reproduces the $H$ and $K$ portions of CHARIS spectrum and the NIRC2 $L_p$ photometry; however, it underpredicts the brightness of HIP 109427 B in $Y$ and $J$ band by 85% and 25%, respectively. Subsolar metallicity models

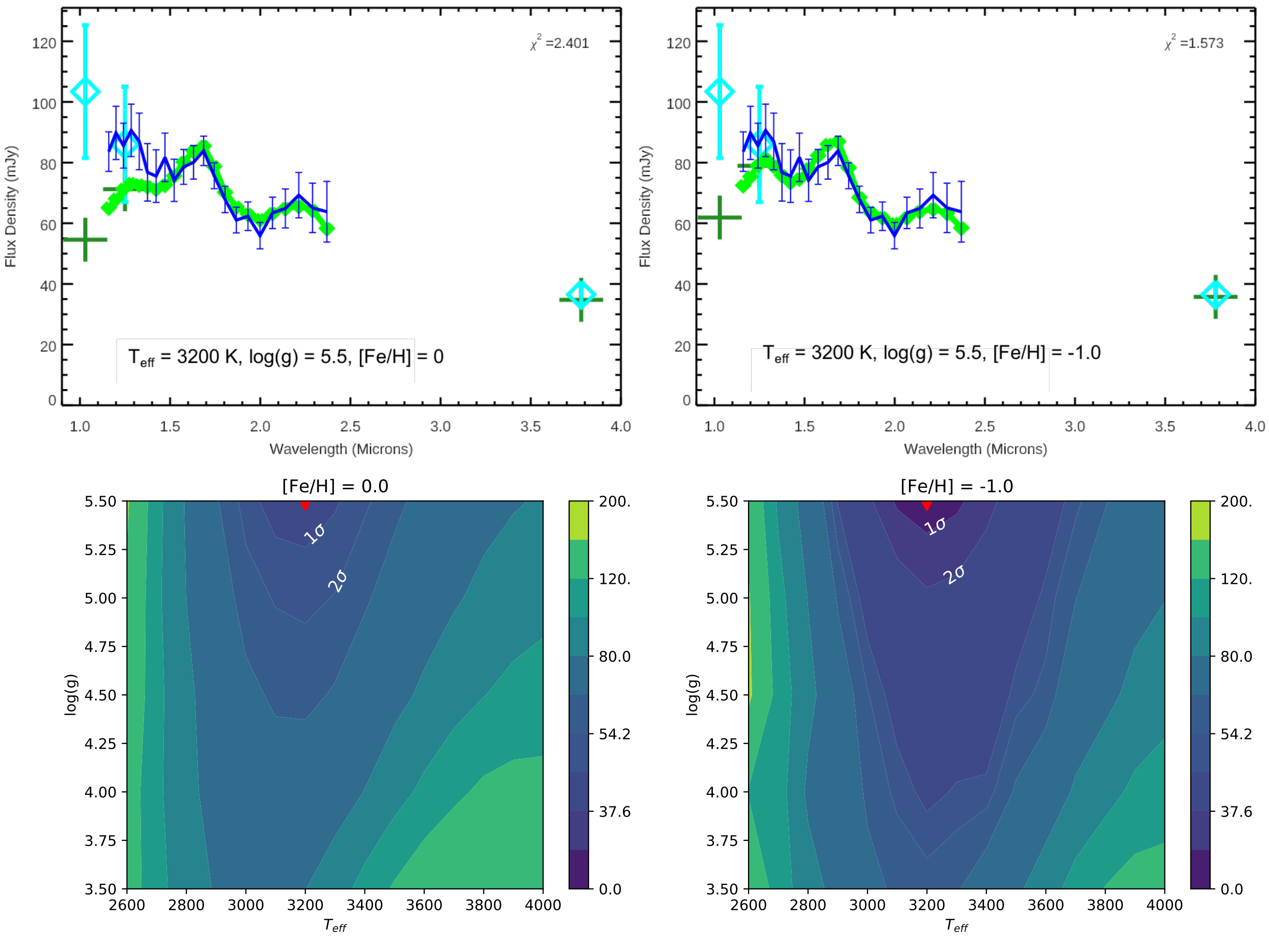


**Figure 5.** (top) Best fit BT-Settl models for a solar and non-solar metallicity and (bottom) corresponding contour plots of $\chi^2$ as a function of temperature and surface gravity. The 1$\sigma$ and 2$\sigma$ contours are labeled in white and the best fit solution denoted with a red diamond. The $\chi^2_\nu$ value shown is for 20 degrees of freedom. CHARIS spectra is shown in blue, MEC and NIRC2 photometry in cyan, model-predicted CHARIS spectrophotometry in light green, and predicted MEC/NIRC2 photometry in dark green.

systematically produce a rough match in $J$ band and show less severe disagreement at $Y$ band. Future MEC calibration work may yield better agreement with expected $Y$ band photometry.

The 2-$\sigma$ ranges for temperature correspond to M3–M5.5 dwarfs, a range that overlaps with the spectral types of best-matching objects in the Montreal Spectral Library, although the best-fit is skewed towards earlier, hotter objects by by ∼1 subclass. For M3–M5.5 objects with the HIP 109427 system's estimated age of $\sim$ 0.4–0.7 *Gyr*, the expected surface gravities are log(g) $\sim$ 5–5.1 (Baraffe et al. 2003), or about 0.25–0.5 dex lower than the best-fit values considered by our grid. Expected radii are 2–3 Jupiter radii: consistent with our best-fit values.

### 4.3. *HIP 109427 B Astrometry and Dynamical Mass*

#### 4.3.1. *Evidence for Common Proper Motion*

To rule out the possibility that HIP 109427 B is a background object, we analyzed archival 2015 Keck/NIRC2 data shown in Figure 6. The data do not reveal a statistically significant detection of any signal that could be HIP 109427 B. We estimate a 5-$\sigma$ contrast of $\Delta L_{\rm p} \sim 5$, 5.75, 11.3, and 12 magnitudes at 0.″15, 0.″225, 1.″0, and 1.″5, respectively. Companions at HIP 109427 B's current angular separation would be just undetectable at 5-$\sigma$. Those with contrasts like HIP 109427 B near 2 $\lambda$/D would be well below the detection limit and those at arcsecond or wider separations would be easily detected.

HIP 109427 has an extremely high proper motion of $\mu_\alpha\ cos(\delta)$, $\mu_\delta \sim 282.18$, 30.46 mas yr$^{-1}$ (van Leeuwen 2007). If HIP 109427 B were a background star, it would appear at an angular separation of ∼1.″6 in October 2015 data with an expected SNR of $\sim$ 1000. However, no signal is present at its expected location (dashed circle).

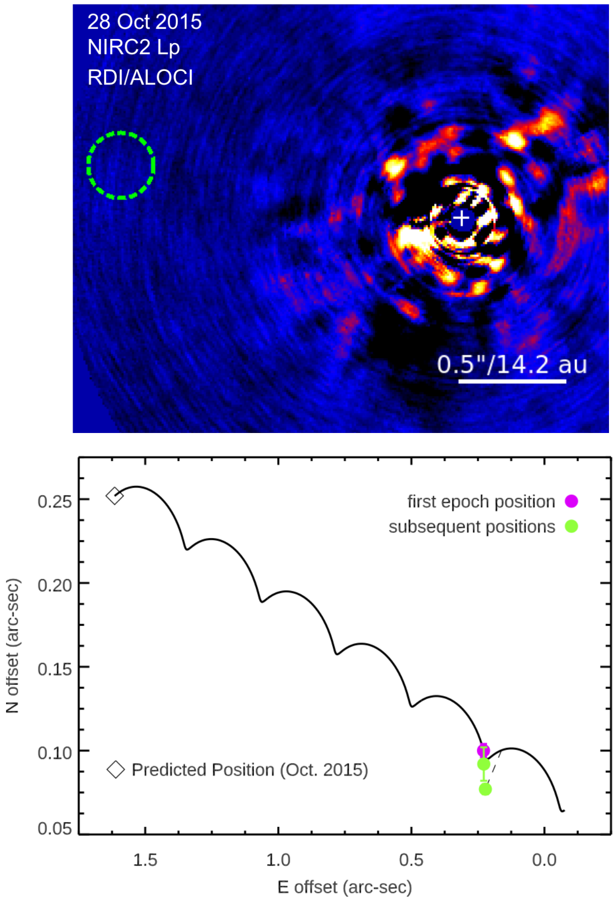


**Figure 6.** (top) Keck/NIRC2 data taken in $L_p$ showing a non-detection at the expected location of the companion, which is circled in green. (bottom) Expected track for a background object showing its predicted location in October 2015. The dashed line connects the measured Dec 2020 position to the predicted position for a background object.

HIP 109427 B's position in December 2020 also deviates by $\sim$ 65 mas compared to the expected location of a background star, far larger than our astrometric precision (bottom panel). This implies HIP 109427 B is a common proper motion companion to the primary.

#### 4.3.2. *Orbit and Dynamical Mass*

We used the open source code `orvara`, Brandt & et al. (2021 - submitted), to fit the mass and orbit of HIP 109427 B using HGCA absolute astrometry measurements for the star and the three measured epochs of relative astrometry for the companion from CHARIS and MEC. We do not consider RV limits, since previous data has had a limited time baseline and poor precision. A Gaussian prior of $2.1 \pm 0.15$ $M_{\odot}$ was chosen for the primary in concordance with literature values derived from isochrone fitting (Stone et al. 2018; David & Hillenbrand 2015; De Rosa et al. 2014).

**Table 3.** HIP 109427 B Orbit Fitting Results and Priors

| Parameter | Fitted Value | Prior |
|---|---|---|
| $M_{pri}$ ($M_{\odot}$) | $2.09 \pm 0.16$ | Gaussian, $2.1 \pm 0.15$ |
| $M_{sec}$ ($M_{\odot}$) | $0.280^{+0.18}_{-0.059}$ | $1/M_{sec}$ |
| Semimajor axis $a$ (au) | $6.55^{+3.0}_{-0.48}$ | 1/a |
| Eccentricity $e$ | $0.54^{+0.28}_{-0.15}$ | uniform |
| Inclination $i$ (°) | $66.7^{+8.5}_{-14}$ | $\sin(i)$ |

Note—Posterior distributions for the secondary mass and semi-major axis are bimodal with a favored solution of $\sim 0.25$ $M_{\odot}$ and $\sim$ 6 au - see Figure 7 and text for more details.

Figure 7 shows the posterior distributions of select orbital parameters as well as the primary and secondary mass. A summary of the fit parameters can also be found in Table 3. The mass of the primary is nearly identical to the adopted prior with a value of $2.09^{+0.16}_{-0.16}$ $M_{\odot}$ and the fit secondary mass is $0.280^{+0.18}_{-0.059}$ $M_{\odot}$. The best fit eccentricity is $0.54^{+0.28}_{-0.15}$ with an inclination of $66.7^{+8.5}_{-14}$ degrees. The best fit semimajor axis is $6.55^{+3.0}_{-0.48}$ au, although the distribution is bimodal with HIP 109427 B's mass with one family of solutions favoring a $\sim$6 au separation with a mass of $\sim$ 0.25 $\pm$ 0.05 $M_{\odot}$ and another favoring a mass of 0.5 $M_{\odot}$ and semimajor axis of 9 au. Main-sequence stars with masses of 0.5 $M_{\odot}$ have early M spectral types (e.g. Pecaut & Mamajek 2013), which are excluded from our spectral analysis. In contrast, the lower-mass solution is consistent with M4 V object allowed by the CHARIS spectral comparisons.

A mass of $\sim$0.25 $M_{\odot}$ is broadly consistent with inferred masses based on luminosity evolution models, given HIP 109427 B's likely age. From the Baraffe et al. (2003) models, an M3–M5.5 object with an age of 400–700 $Myr$ is predicted to have a mass of 0.15–0.3 $M_{\odot}$. Modeling absolute astrometry of the primary and relative astrometry of the star likely then yields much more precise (20%) constraints on the companion mass than available from luminosity evolution models alone (50%).

## 5. DISCUSSION

With SCExAO/MEC photometry, SCExAO/CHARIS spectroscopy, and Keck/NIRC2 photometry, we have identified a low mass stellar companion at a near-Jupiter-like separation around the nearby A1V star HIP 109427. Comparison of this target's spectrum with entries in the Montreal Spectral Library indicates a spectral type of M4–M5.5. This is consistent with a best fit a dynamical mass of $\sim$ 0.25 $M_{\odot}$ with a semimajor axis of $\sim$ 6 au from orbital fitting using measurements from both *Hipparcos* and *Gaia* DR2 as well as MEC, CHARIS, and NIRC2 relative astrometry. There is a degeneracy in the orbital fit with another favored solution of $\sim 0.5\ M_\odot$ with a semimajor axis of $\sim 9$ au that is excluded by our spectral analysis. Future RV measurements, Gaia astrometry, and relative astrometry from high-contrast imaging will help to better constrain this orbit.

This result demonstrates the efficacy of Stochastic Speckle Discrimination (SSD) in identifying faint companions. SSD increases the SNR of HIP 109427 B by about a factor of 3 versus the total intensity image (comparable to the CHARIS SNR of this target) without the use of any additional PSF subtraction techniques. This technique is especially effective at small angular separations (inside 10 $\lambda$/D) where algorithms exploiting traditional observing strategies like ADI and SDI suffer.

Work expanding the SSD framework to be agnostic to bin size and to directly fit an off-axis Poisson source has been shown to be effective on simulated data and is currently being adapted for use on real datasets (Walter et al. 2019). This will allow the SSD technique to directly extract the component of the intensity attributable to the companion itself. This information could then be fed into other traditional post-processing techniques (such as ADI and SDI) to further improve the SNR of faint companion detections.

## 6. ACKNOWLEDGEMENTS

Sarah Steiger and Neelay Fruitwala are supported by a grant from the Heising-Simons Foundation. Kristina K. Davis is supported by the NSF Astronomy and Astrophysics Postdoctoral Fellowship program under award # 1801983. Jennifer P. Smith and Nicholas Zobrist are both supported by a NASA Space Technology Research Fellowship. Isabel Lipartito is supported by the National Science Foundation Graduate Research Fellowship under grant # 1650114. Thayne Currie was supported by a NASA Senior Postdoctoral Fellowship and NASA/Keck grant LK-2663-948181. M.T. is supported by JSPS KAKENHI grant # 18H05442, # 15H02063, and # 22000005.

We thank the Subaru and NASA Keck Time Allocation Committees for their generous support of this program and Chas Beichman and Dawn Gelino for graciously supporting additional NIRC2 time. This work makes use of the Keck Observatory Archive (KOA), a joint development between the W. M. Keck Observatory and the NASA Exoplanet Science Institute (NExScI). CHARIS was built at Princeton University under a Grant-in-Aid for Scientific Research on Innovative Areas from MEXT of the Japanese government (# 23103002)

The development of SCExAO was supported by the Japan Society for the Promotion of Science (Grant-in-Aid for Research #23340051, #26220704, #23103002, #19H00703 & #19H00695), the Astrobiology Center of the National Institutes of Natural Sciences, Japan, the Mt Cuba Foundation and the director's contingency fund at Subaru Telescope. The authors wish to recognize and acknowledge the very significant cultural role and reverence that the summit of Maunakea has always had within the indigenous Hawaiian community, and are most fortunate to have the opportunity to conduct observations from this mountain.

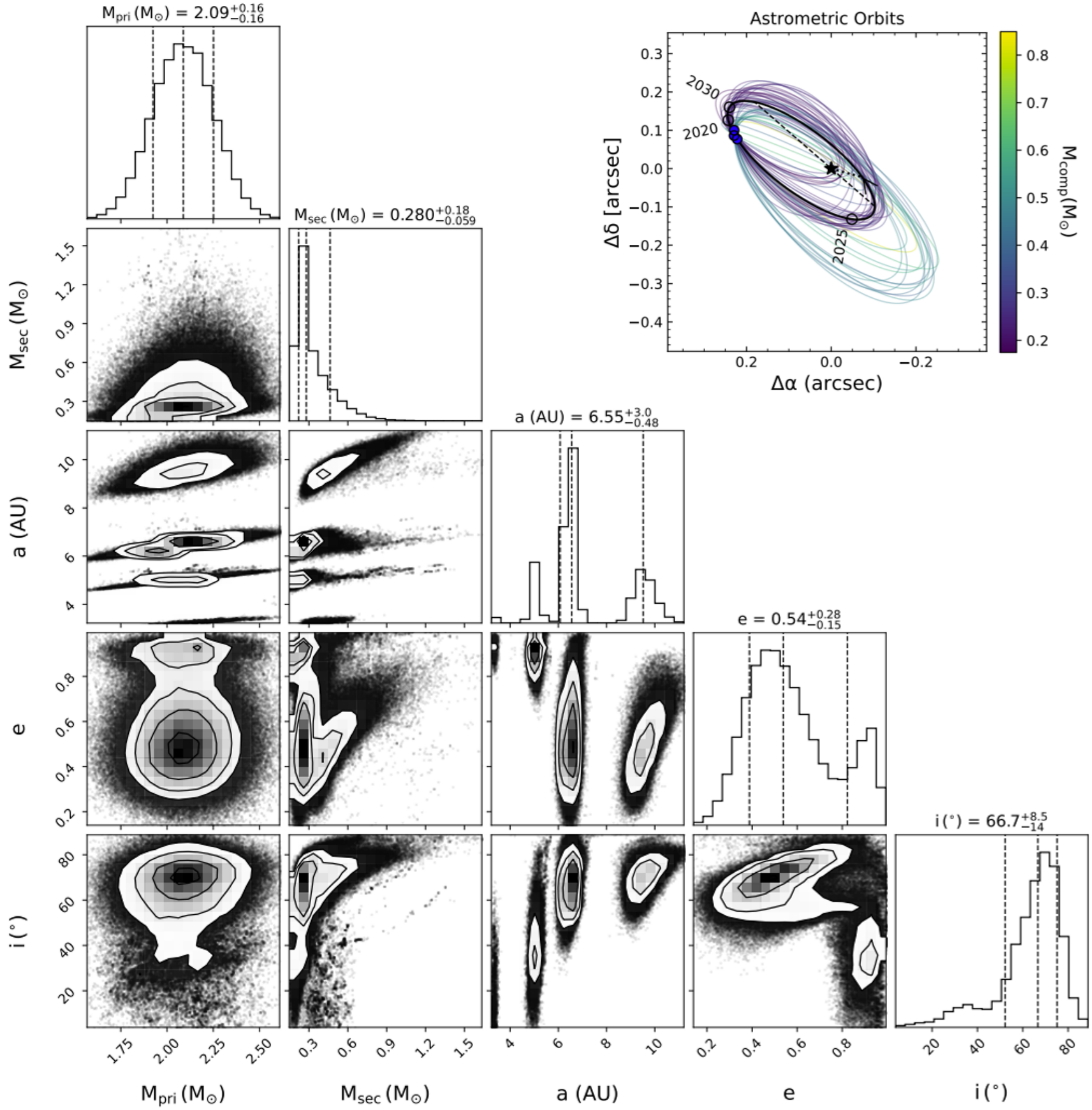


**Figure 7.** Corner plot displaying select posterior orbital parameters. The orbit fits were performed using HGCA data and relative astrometry points from SCExAO/CHARIS and MEC data. The mass of the primary is nearly identical to the chosen prior of $2.1^{+0.15}_{-0.15}$ $M_\odot$. (Inset) The best fit orbit of HIP 109427 B in black with 50 randomly selected orbits from the MCMC fit color-coded by HIP 109427 B's mass. The blue circles represent the measured relative astrometry points and the unfilled black circles are the predicted locations of the companion at different epochs. The arrow indicates that HIP 109427 B is orbiting counter-clockwise

## REFERENCES


Allard, F., Homeier, D., & Freytag, B. 2012, Philosophical Transactions of the Royal Society of London Series A, 370, 2765, doi: 10.1098/rsta.2011.0269

Asplund, M., Grevesse, N., Sauval, A. J., & Scott, P. 2009, ARA&A, 47, 481, doi: 10.1146/annurev.astro.46.060407.145222

Baraffe, I., Chabrier, G., Barman, T. S., Allard, F., & Hauschildt, P. H. 2003, A&A, 402, 701, doi: 10.1051/0004-6361:20030252

Beuzit, J. L., Vigan, A., Mouillet, D., et al. 2019, A&A, 631, A155, doi: 10.1051/0004-6361/201935251

Bond, C. Z., Cetre, S., Lilley, S., et al. 2020, Journal of Astronomical Telescopes, Instruments, and Systems, 6, 039003, doi: 10.1117/1.JATIS.6.3.039003

Brandt, T. D. 2018, ApJS, 239, 31, doi: 10.3847/1538-4365/aaec06

Brandt, T. D., & et al. 2021 - submitted, ApJ

Brandt, T. D., Rizzo, M., Groff, T., et al. 2017, Journal of Astronomical Telescopes, Instruments, and Systems, 3, 048002, doi: 10.1117/1.JATIS.3.4.048002

Cagigal, M. P., & Canales, V. F. 2001, Optical Engineering, 40, 2690, doi: 10.1117/1.1417495

Casagrande, L., Flynn, C., & Bessell, M. 2008, MNRAS, 389, 585, doi: 10.1111/j.1365-2966.2008.13573.x

Chauvin, G., Desidera, S., Lagrange, A. M., et al. 2017, A&A, 605, L9, doi: 10.1051/0004-6361/201731152

Currie, T., Cloutier, R., Brittain, S., et al. 2015, ApJL, 814, L27, doi: 10.1088/2041-8205/814/2/L27

Currie, T., Daemgen, S., Debes, J., et al. 2014, ApJL, 780, L30, doi: 10.1088/2041-8205/780/2/L30

Currie, T., Burrows, A., Itoh, Y., et al. 2011, ApJ, 729, 128, doi: 10.1088/0004-637X/729/2/128

Currie, T., Debes, J., Rodigas, T. J., et al. 2012, ApJL, 760, L32, doi: 10.1088/2041-8205/760/2/L32

Currie, T., Brandt, T. D., Uyama, T., et al. 2018a, AJ, 156, 291, doi: 10.3847/1538-3881/aae9ea

Currie, T., Kasdin, N. J., Groff, T. D., et al. 2018b, PASP, 130, 044505, doi: 10.1088/1538-3873/aaab41

Currie, T., Marois, C., Cieza, L., et al. 2019, ApJL, 877, L3, doi: 10.3847/2041-8213/ab1b42

Currie, T., Brandt, T. D., Kuzuhara, M., et al. 2020a, ApJL, 904, L25, doi: 10.3847/2041-8213/abc631

Currie, T., Guyon, O., Lozi, J., et al. 2020b, arXiv e-prints, arXiv:2012.05241. https://arxiv.org/abs/2012.05241

David, T. J., & Hillenbrand, L. A. 2015, ApJ, 804, 146, doi: 10.1088/0004-637X/804/2/146

De Rosa, R. J., Patience, J., Wilson, P. A., et al. 2014, MNRAS, 437, 1216, doi: 10.1093/mnras/stt1932

De Rosa, R. J., Rameau, J., Patience, J., et al. 2016, ApJ, 824, 121, doi: 10.3847/0004-637X/824/2/121

Ducati, J. R. 2002, VizieR Online Data Catalog

Fitzgerald, M. P., & Graham, J. R. 2006, ApJ, 637, 541, doi: 10.1086/498339

Gagné, J., Faherty, J. K., Cruz, K. L., et al. 2015, ApJS, 219, 33, doi: 10.1088/0067-0049/219/2/33

Gagné, J., Mamajek, E. E., Malo, L., et al. 2018, ApJ, 856, 23, doi: 10.3847/1538-4357/aaae09

Give'on, A., Kern, B., Shaklan, S., Moody, D. C., & Pueyo, L. 2007, in Society of Photo-Optical Instrumentation Engineers (SPIE) Conference Series, Vol. 6691, Astronomical Adaptive Optics Systems and Applications III, ed. R. K. Tyson & M. Lloyd-Hart, 66910A, doi: 10.1117/12.733122

Gladysz, S., & Christou, J. C. 2008, ApJ, 684, 1486, doi: 10.1086/589679

—. 2009, ApJ, 698, 28, doi: 10.1088/0004-637X/698/1/28

Gonzaga, S., Hack, W., Fruchter, A., & Mack, J. 2012, The DrizzlePac Handbook

Goodman, J. W. 1975, Statistical properties of laser speckle patterns, ed. J. C. Dainty, Vol. 9, 9, doi: 10.1007/BFb0111436

Gray, R. O., Corbally, C. J., Garrison, R. F., et al. 2006, AJ, 132, 161, doi: 10.1086/504637

Greco, J. P., & Brandt, T. D. 2016, ApJ, 833, 134, doi: 10.3847/1538-4357/833/2/134

Groff, T. D., Chilcote, J., Kasdin, N. J., et al. 2016, in Society of Photo-Optical Instrumentation Engineers (SPIE) Conference Series, Vol. 9908, Ground-based and Airborne Instrumentation for Astronomy VI, 99080O, doi: 10.1117/12.2233447

Guyon, O. 2005, ApJ, 629, 592, doi: 10.1086/431209

Howard, A. W., & Fulton, B. J. 2016, PASP, 128, 114401, doi: 10.1088/1538-3873/128/969/114401

Jovanovic, N., Guyon, O., Martinache, F., et al. 2015a, ApJL, 813, L24, doi: 10.1088/2041-8205/813/2/L24

Jovanovic, N., Martinache, F., Guyon, O., et al. 2015b, PASP, 127, 890, doi: 10.1086/682989

Kuzuhara, M., Tamura, M., Kudo, T., et al. 2013, ApJ, 774, 11, doi: 10.1088/0004-637X/774/1/11

Lafrenière, D., Marois, C., Doyon, R., Nadeau, D., & Artigau, É. 2007, ApJ, 660, 770, doi: 10.1086/513180

Lagrange, A. M., Desort, M., Galland, F., Udry, S., & Mayor, M. 2009, A&A, 495, 335, doi: 10.1051/0004-6361:200810105

Lozi, J., Guyon, O., Jovanovic, N., et al. 2018, Journal of Astronomical Telescopes, Instruments, and Systems, 4, 049001, doi: 10.1117/1.JATIS.4.4.049001

Macintosh, B., Graham, J. R., Ingraham, P., et al. 2014, Proceedings of the National Academy of Science, 111, 12661, doi: 10.1073/pnas.1304215111

Macintosh, B., Graham, J. R., Barman, T., et al. 2015, Science, 350, 64, doi: 10.1126/science.aac5891

Makarov, V. V., & Kaplan, G. H. 2005, AJ, 129, 2420, doi: 10.1086/429590

Males, J. R., Close, L. M., Guyon, O., et al. 2020, in Society of Photo-Optical Instrumentation Engineers (SPIE) Conference Series, Vol. 11448, Society of Photo-Optical Instrumentation Engineers (SPIE) Conference Series, 114484L, doi: 10.1117/12.2561682

Marois, C., Doyon, R., Racine, R., & Nadeau, D. 2000, PASP, 112, 91, doi: 10.1086/316492

Marois, C., Lafrenière, D., Doyon, R., Macintosh, B., & Nadeau, D. 2006, ApJ, 641, 556, doi: 10.1086/500401

Marois, C., Lafrenière, D., Macintosh, B., & Doyon, R. 2008a, ApJ, 673, 647, doi: 10.1086/523839

Marois, C., Macintosh, B., Barman, T., et al. 2008b, Science, 322, 1348, doi: 10.1126/science.1166585

Mawet, D., Pueyo, L., Lawson, P., et al. 2012, in Society of Photo-Optical Instrumentation Engineers (SPIE) Conference Series, Vol. 8442, Space Telescopes and Instrumentation 2012: Optical, Infrared, and Millimeter Wave, ed. M. C. Clampin, G. G. Fazio, H. A. MacEwen, & J. Oschmann, Jacobus M., 844204, doi: 10.1117/12.927245

Mawet, D., Milli, J., Wahhaj, Z., et al. 2014, ApJ, 792, 97, doi: 10.1088/0004-637X/792/2/97

Mazin, B. A., Bumble, B., Meeker, S. R., et al. 2012, Optics Express, 20, 1503, doi: 10.1364/OE.20.001503

Meeker, S. R., Mazin, B. A., Walter, A. B., et al. 2018, PASP, 130, 065001, doi: 10.1088/1538-3873/aab5e7

Millar-Blanchaer, M. A., Perrin, M. D., Hung, L.-W., et al. 2016, in Society of Photo-Optical Instrumentation Engineers (SPIE) Conference Series, Vol. 9908, Ground-based and Airborne Instrumentation for Astronomy VI, ed. C. J. Evans, L. Simard, & H. Takami, 990836, doi: 10.1117/12.2233071

Nielsen, E. L., De Rosa, R. J., Macintosh, B., et al. 2019, AJ, 158, 13, doi: 10.3847/1538-3881/ab16e9

Pecaut, M. J., & Mamajek, E. E. 2013, ApJS, 208, 9, doi: 10.1088/0067-0049/208/1/9

Perrin, M. D., Sivaramakrishnan, A., Makidon, R. B., Oppenheimer, B. R., & Graham, J. R. 2003, ApJ, 596, 702, doi: 10.1086/377689

Pueyo, L. 2016, ApJ, 824, 117, doi: 10.3847/0004-637X/824/2/117

Rameau, J., Chauvin, G., Lagrange, A. M., et al. 2013, ApJL, 779, L26, doi: 10.1088/2041-8205/779/2/L26

Sahoo, A., Guyon, O., Lozi, J., et al. 2020, AJ, 159, 250, doi: 10.3847/1538-3881/ab88cd

Serabyn, E., Huby, E., Matthews, K., et al. 2017, AJ, 153, 43, doi: 10.3847/1538-3881/153/1/43

Soummer, R., Ferrari, A., Aime, C., & Jolissaint, L. 2007, ApJ, 669, 642, doi: 10.1086/520913

Soummer, R., Pueyo, L., & Larkin, J. 2012, ApJL, 755, L28, doi: 10.1088/2041-8205/755/2/L28

Stone, J. M., Skemer, A. J., Hinz, P. M., et al. 2018, AJ, 156, 286, doi: 10.3847/1538-3881/aaec00

Szypryt, P., Meeker, S. R., Coiffard, G., et al. 2017, Optics Express, 25, 25894, doi: 10.1364/OE.25.025894

van Leeuwen, F. 2007, A&A, 474, 653, doi: 10.1051/0004-6361:20078357

Vigan, A., Fontanive, C., Meyer, M., et al. 2020, arXiv e-prints, arXiv:2007.06573. https://arxiv.org/abs/2007.06573

Walter, A. B., Bockstiegel, C., Brandt, T. D., & Mazin, B. A. 2019, PASP, 131, 114506, doi: 10.1088/1538-3873/ab389a

Walter, A. B., Fruitwala, N., Steiger, S., et al. 2020, PASP, 132, 125005, doi: 10.1088/1538-3873/abc60f